Wear 358-359 (2016) 109–122

Contents lists available at ScienceDirect

Wear

journal homepage: www.elsevier.com/locate/wear

Water droplet erosion behaviour of Ti–6Al–4V and mechanisms of material damage at the early and advanced stages

A.K. Gujba [a], L. Hackel [b], D. Kevorkov [a], M. Medraj [a,c,*]

[a] Department of Mechanical and Industrial Engineering, Concordia University, 1455 De Maisonneuve Blvd. W. Montreal, Quebec, Canada, H3G 1M8
[b] Metal Improvement Company-Curtiss Wright Corporation, 7655 Longard Road, Livermore, CA 94551, United States
[c] Department of Mechanical and Materials Engineering, Masdar Institute, P.O. Box 54224, Masdar City, Abu Dhabi, United Arab Emirates

ARTICLE INFO

Article history:
Received 15 December 2015
Received in revised form
5 April 2016
Accepted 7 April 2016
Available online 14 April 2016

Keywords:
Water droplet erosion
Impact speed
Incubation stage
Advanced stage
Ti–6Al–4V

ABSTRACT

In this study, the water droplet erosion (WDE) behaviour of Ti–6Al–4V and mechanisms of material damage were investigated. The WDE test was conducted in an advanced rig in accordance with the ASTM G73 standard. The influence of impact speed between 150 and 350 m/s on the WDE behaviour was explored and the cumulative mass losses *versus* the exposure time/number of impingements were plotted. It was observed that the higher the impact speed the faster the erosion initiation time and greater the maximum erosion rate (ER_{max}). ER_{max} was also found to be related to the impact speed with an exponent of 9.9 in a log–log scale. SEM images showed that the early stages of erosion damage were mainly limited to the formation of microcracks, asperities and isolated pits of irregular shapes. It was found that the most profound mode of material removal during the advanced stage of water droplet erosion was hydraulic penetration. Sub-surface, side wall cracking and material folding/upheaving were also features observed.

1. Introduction

In the electric power generation industry the gas turbine efficiency is an important issue and is directly affected by the ambient temperature. Meher-Homji and Mee [1] reported that a rise of 1 °F results in a 0.3–0.5% in turbine efficiency decrease. This adverse temperature effect is obviously a season-dependent phenomenon. For instance, in the United States, a 9% loss of gas turbine output power was recorded in summer *versus* winter periods [2]. The lower turbine efficiency is attributed to a decrease in air density leading to a decrease in the intake air mass [3]. The lower efficiency results in high electricity cost [4] and high CO_2 emissions [3]. To keep the ambient temperature as low as possible, the inlet air fog cooling technique is used [1]. In this technique, water droplets are sprayed into the inlet of the gas turbine compressor to cool down the intake air thereby increasing the intake mass. The water droplets reduce the temperature leading to an increase in the output power [5]. However, an overspray can occur when all droplets are not evaporated [5,6]. Despite the cost effectiveness of this fogging method, droplets cause a severe erosion damage problem for the leading edge of the compressor blades and consequently a significant fatigue cracking issue for the full blades, especially at high speeds. Khan [6] stated that the erosion damage phenomenon was featured as the synergy of the impacting water droplets and the rotating blade. This is usually termed as the "water erosion by impingement or water droplet erosion (WDE)".

Water erosion by impingement is a special form of erosion produced by repetitive impingement of high velocity liquid droplets on a solid surface [7]. The mechanism of the erosion process is complex because of the many parameters involved, including: impact velocity, impact angle, droplet size, droplet density, frequency of impacts, liquid film formation and mechanical properties and conditions of the target material. However, this erosion phenomenon has also been found in several industrial applications including cooling pipes of nuclear plants [8], sewage plants and sea water systems [9], aerodynamic surfaces of aircrafts and missiles [10] flying through rainstorm at subsonic and supersonic speeds [11]. The WDE damage is predominantly caused by two main factors: (1) the high pressure exerted by the water droplet on the exposed area of the solid surface and (2) the radial liquid flow along the surface at high-speed, which occurs after the initial droplet pressure lessens [11]. Moreover, this erosion damage reduces the efficiency of mechanical components due to aerodynamic losses [12]. Despite the efforts to combat or mitigate the erosion damage, it has not been possible to identify or quantify an absolute parameter for WDE resistance [10]. This is due to the fact that erosion rate is not constant with time and therefore, no single

* Corresponding author at: Department of Mechanical and Industrial Engineering, Concordia University, 1455 De Maisonneuve Blvd. W. Montreal, Quebec, Canada, H3G 1M8. Tel.: +1 514 848 2424x3146; fax: +1 514 848 3175.
E-mail address: mmedraj@encs.concordia.ca (M. Medraj).

http://dx.doi.org/10.1016/j.wear.2016.04.008
0043-1648/

value can quantify the erosion test. Significant attempts have been made to attribute the hardness [11], toughness [11], work hardening [13], and ultimate resilience [14] to the WDE resistance. More so, a synergistic effect of these parameters would be a more appropriate term. For this reason, the material (rating) ranking system which is somewhat semi-quantitative has been developed by Heymann [15]. He [15] proposed sets of comparative studies in order to evaluate erosion resistance under different sets of conditions. In this system, the normalized erosion resistance, which is the maximum rate of volume loss of a reference material divided by the maximum rate of volume loss of material being evaluated, is calculated. However, the major setback here is the lack of precision in projecting the erosion damage. ASTM standard [10] mentioned that for bulk materials, the incubation period and the maximum erosion rate determined from empirical relationships could be used for the material rating; provided, the principal liquid impingement parameters such as droplet size, impact velocity are known. Also, due to the variation of erosion rate with exposure time and synergy of different interacting WDE parameters such as impact speed and droplet size, different WDE behaviours and damage mechanisms will prevail. Thus, predicting or projecting the erosion damage becomes difficult. In this case, the experimental investigations become paramount. The mechanism by which a material is removed or chipped out is an important aspect of the WDE damage. However, the challenge lies in defining the hydrodynamic conditions that cause particular erosion and material detachment effects [11]. Nevertheless, it is paramount to fully understand the WDE behaviour of materials and the mechanism by which a material is removed when exposed to an erosive medium. To understand this, the concept of water hammer pressure, stress wave propagation, liquid outflow and hydraulic penetration as well as material response must be comprehended.

In this study, the WDE behaviour of Ti–6Al–4V and the mechanism of material removal during the early and advanced stages of erosion damage were investigated. Special attention was given to the influence of impact speed of the erosion behaviour. Cumulative mass loss, number of impingements, erosion initiation time and maximum erosion rate (ER_{max}) with respect to the impact speed were derived. Study on the mechanism of material removal was conducted with the aid of a scanning electron microscope (SEM). Here, the as-eroded surface and polished cross-sectional views were investigated.

2. Experimental procedure

2.1. Material and geometry

For the present study, the Ti–6Al–4V (ASTM B265, Grade 5) alloy, used for compressor blades in gas turbine, was investigated. Typical room temperature physical and mechanical properties are: elastic modulus (113 GPa), Poisson's ratio (0.342), melting point temperature range (1604–1660 °C) and tensile strength (880 MPa). T-shaped coupons, as shown in Fig. 1, were machined using a CNC Haas machine under flood coolant in accordance to the WDE testing rig geometry. Fig. 2 shows the starting microstructure of the Ti–6Al–4V alloy which contains α and β phases.

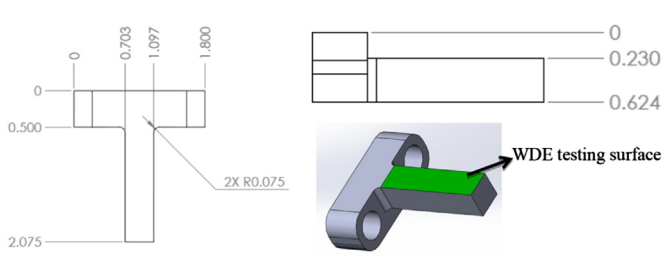

Fig. 1. Typical T-shaped Ti–6Al–4V sample (dimensions are in inches).

2.2. WDE testing, mass loss measurement and characterization of eroded coupons

A state-of-the-art rotating disc rig at Concordia University, shown in Fig. 3, was used for studying the WDE behaviour of the Ti–6Al–4V alloy. The test was carried out in accordance with ASTM G73 standard [10]. This is a unique testing rig that reaches up to 500 m/s linear speed (equivalent to 20,000 rpm rotational speed). It has a working chamber coupled with a vacuum system, a compressed air driven turbine and a water droplet generating system. The rig has a user friendly control system allowing monitoring of the vibration level, vacuum level, chamber temperature, turbine bearing temperature as well as the rotational speed. Coupons are fixed at the opposite ends of the rotating disc as depicted in Fig. 3.

To avoid friction between the rotating disc and air, which causes significant temperature rise, a 30–50 mbar vacuum is maintained during the experiment. Thus, favourable working temperature was maintained and water evaporation was avoided. This vacuuming approach further allows for WDE testing at very high impact speeds. It is worth mentioning that a separate setup using a transparent chamber was used to simulate the water droplets behaviour inside the rig. The droplet size distribution was monitored using a high-speed camera (9000 frames per second) with the aid of this setup. Furthermore, the number of droplets was counted which was essential for computing other parameters such as the volume of impinging water. Similar water droplet generation and size distribution determination has been reported in [16–18]. Typical WDE testing parameters are summarized in Table 1. Once a desired rotational speed was attained, the water droplets (de-ionized water) were introduced while controlling the flow rate. The setup enabled the droplets to impact the coupons at 90° in a repetitive fashion. The impact angle of 90° causes the most severe water erosion damage. The erosion exposure time depended on the impact speed used. However, timings at 30 s intervals were used in order to capture the first stage of the erosion process (incubation period). Also, longer times (1, 2, 3 up to 840 min) were employed as the test progressed to the advanced stage of the erosion process.

Coupons were weighed using a balance and pictures were taken with a standard stereo optical microscope, at each interval. Typical erosion curves such as cumulative mass loss *versus* exposure time/number of impingement and ER_{max} *versus* impact speed were plotted. For accurate determination of the incubation period and maximum erosion rate, a three line representation method was used as demonstrated in Fig. 4 [19]. The mechanism of material removal during the incubation and advanced stages was monitored and the damages were characterized using SEM. Here, the as-eroded surface and polished cross-sectional views were investigated. Microcracks, stress wave propagation, crack initiation sites, formation of pits and removal of cavity were primarily investigated. Results and discussion are presented in the next section.

3. Results and discussion

3.1. Droplets generation and size distribution

Prior to the WDE tests, several experiments were performed with an impact angle of 90° in order to establish and calibrate the erosion test conditions, such as initial pressure, flow rate and droplet size distribution. Droplet generating system and a nozzle

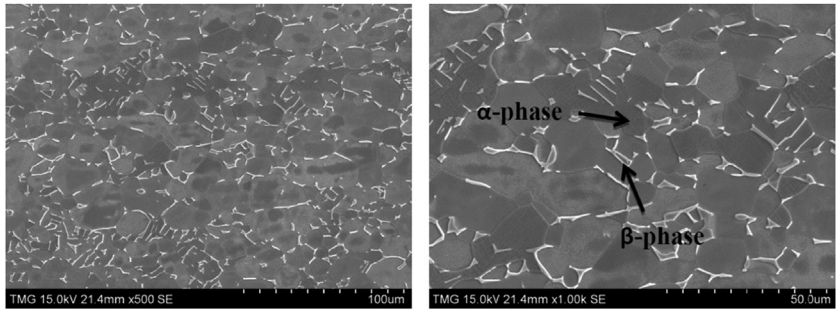

Fig. 2. SEM micrographs showing the initial Ti–6Al–4V microstructure.

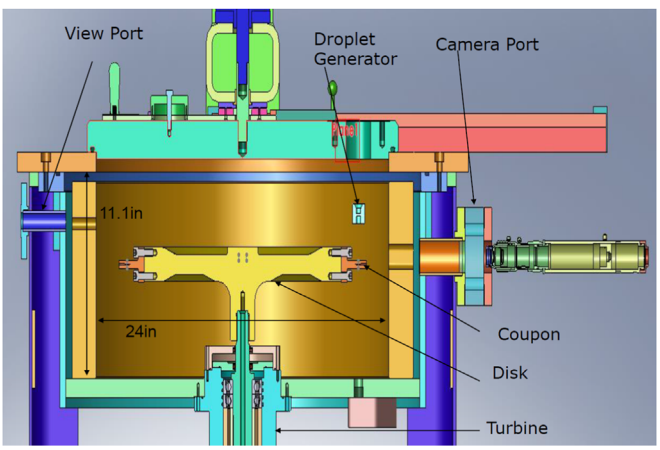

Fig. 3. Schematic illustration of the water erosion rig used in the present work.

Table 1
WDE test parameters used in this work.

Process parameter	Variable
Impact speed (m/s)	150, 200, 250, 275, 300, 325, 350
Rotational speed × 10^3 (rpm)	6, 8, 10, 11, 12, 13, 14
Flow rate (l/min)	0.05
Nozzle distance from coupon (mm)	5
Average droplet size (μm)	463
Initial pressure (mbar)	30–50
Impact angle (°)	90

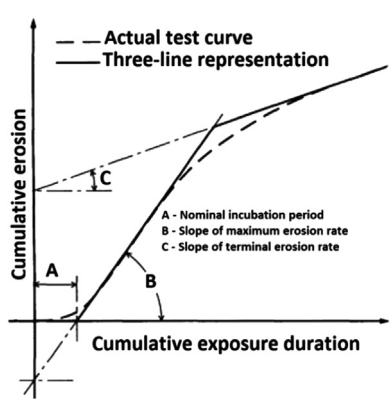

Fig. 4. Typical three line representation for WDE curve characterization [19].

were used to produce a streak of water droplets. The generated droplets and sizes depend on the water line pressure, nozzle diameter and flow rate [16]. In this study, water line pressure of 1 psi, flow rate of 0.05 l/min and nozzle diameter of 400 μm were used. The diameters of the droplets were measured and a statistical distribution of 200 droplet diameter counts was derived as shown in Fig. 5a. Fig. 5a indicates that the droplet size range was between 400 and 527 μm with an average size of 463 μm. In addition, the observed droplet size range is within the spectrum of size ranges (50–1500 μm) encountered by components subjected to WDE [20,21] and used in similar investigations [13,16–18]. During the off-situ droplet size monitoring, the equivalent number of droplets hitting the coupon surface per revolution was obtained with the aid of a high-speed camera. The number of droplets hitting the surface depends on the dimension of the exposed surface. For instance, Fig. 5b shows that six droplets would be hitting the exposed surface of an 8 mm thick coupon per revolution. This observation and finding indicate that the total number of droplets or volume of water impinging the coupon during testing can be quantified with reasonable degree of accuracy.

3.2. WDE curves and characterization

Water erosion results are typically reported as cumulative material loss *versus* cumulative exposure time [10]. However, "number of impingements" was preferred to cumulative exposure time in this paper. This is because the number of droplets impinging the coupon at a particular time was known (Fig. 5b). Moreover, the exposure time does not quantify the amount of water used, thus, the number of impingements could be employed successfully in representing the experimental results and data. Per contra, this was not the case in earlier WDE studies such as in [14,22,23]. The number of impingements was obtained using Eq. (1).

$$N_{imp} = R \times E_t \times N_{droplets} \quad (1)$$

where N_{imp} is the number of impingement, R is the rotational speed (rpm), E_t is the erosion exposure time (minutes) and $N_{droplets}$ is the number of droplets hitting the coupon per revolution which is six as per Fig. 5b. Contrarily, Kamkar [23] defined the number of impingement as "the number of times the sample intersects the water stream". This definition would render the x-axis cumulative exposure duration inaccurate or underestimated, since only $R \times E_t$ were considered while neglecting $N_{droplets}$. It is worth noting that the number of droplets impacting the sample varies with droplet size thus, rendering [23]'s estimation more inaccurate. Therefore, it will be difficult to quantify the volume of water injected at a particular time from [23] and the number of impingements to erosion initiation will be underestimated.

The cumulative mass loss can be described as the sum of material loss due to exposure to an erosive medium such as water at a particular time. For better quantification of the mass loss measurement, tested coupons were weighed after each interval. For instance, 30 s intervals up to 2 min were taken initially in order to capture the incubation period (period of negligible mass loss) [19]. It is worth mentioning that the measurable mass losses are

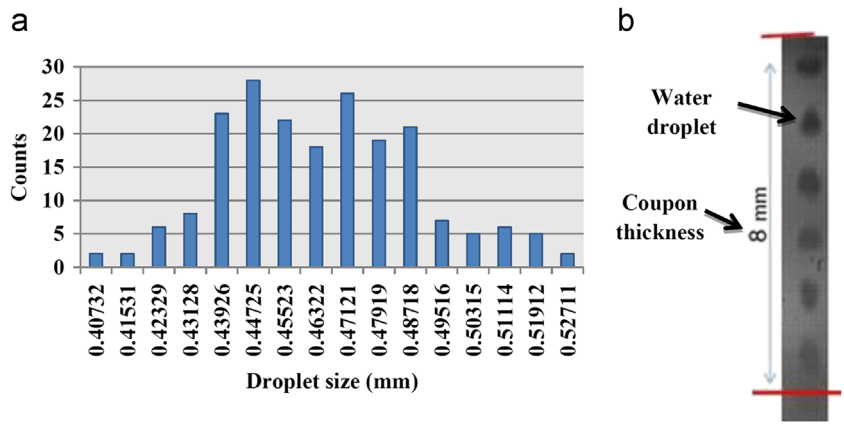

Fig. 5. (a) Statistical distribution of droplet size range and (b) equivalent number of droplets hitting the coupon.

mostly observed when the first threshold velocity (endurance limit) is exceeded after a certain number of impacts [24]. Therefore, the first threshold velocity is the velocity below which no damages (significant mass losses) are observed. The cumulative mass loss *versus* the exposure time/number of impingements graphs for the varied speed tests is reported in this work. The WDE curves for impact speeds of 150, 200, 250, 275 and 300, 325, 350 m/s are shown in Fig. 6a and b, respectively. Fig. 6a and b shows that reducing the impact speed delayed the erosion initiation time and reduced the erosion rate. At an impact speed of 150 m/s no erosion was observed after long exposure to the erosive medium. Only an erosion trace line was observed under the optical microscope as shown in the inset macrograph in Fig. 6a. This indicates that the first threshold velocity (impact speed) of the material is greater than or equal to 150 m/s. On the other hand, increasing the speed showed faster erosion initiation and greater erosion rates. More on the effect of speed on the erosion initiation and maximum erosion rate has been discussed in Sections 3.2.1 and 3.2.2, respectively. It is well known that the shape of erosion curves depends on the target material and the erosion condition [10]. For instance, material with a well-behaved erosion curve has an S-shaped erosion curve with distinct erosion stages [10]. These stages are: incubation period with negligible mass loss; acceleration stage (energy accumulation zone [25]) to a maximum rate stage; deceleration (attenuation) stage with declining erosion rate and terminal or final steady state with constant erosion rate [19,24]. These characteristic curves are further affected by surface roughness [16,24], surface properties, microstructure [11], geometry [24], combination of impact speed and droplet size [24]. For instance, Kirols et al. [16] reported that merely polishing the surface prior to WDE tests delayed the erosion initiation and in some cases, the maximum erosion rates in 12% Cr–Steel and Ti–6Al–4V. It can be seen from Fig. 6a that the erosion stages were different after 50×10^5 impingements for impact speeds of 200 and 250 m/s. The stages attained were incubation and maximum erosion for 200 and 250 m/s. This is also consistent with the WDE results of forged Ti–6Al–4V [23]. In this present study, the surface quality/roughness, microstructure and geometry were kept constant. Furthermore, employing the three line representation according to Fig. 4, the erosion curves were characterized and the initiation time and maximum erosion rate were calculated.

3.2.1. Effect of impact speed on the incubation period

The initiation of erosion is an important stage in the erosion process though it is often affected by several factors, such as: surface roughness, impact pressure, velocity and erosion conditions. According to Hoff et al. [26], the predominant factor in the WDE material damage is the impact velocity of the specimen. This

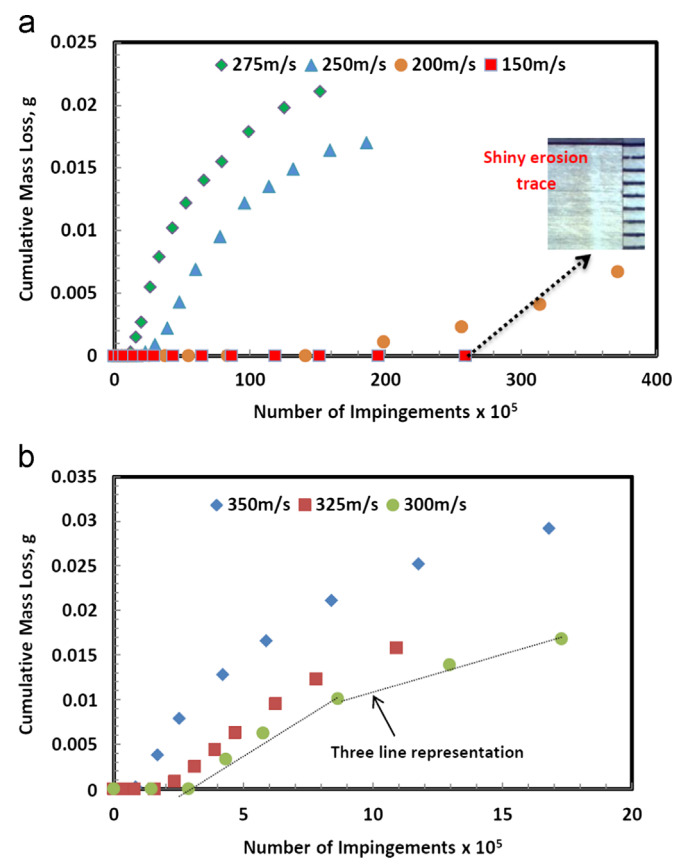

Fig. 6. WDE curves for (a) 150 to 275 m/s and (b) 300 to 350 m/s impact speed tests.

was attributed to the increased kinetic energy with increase in impact velocity (V^2). In real life applications, however, the impact velocity comes from both the movement of the droplet and the rotation of blades. Kiel et al. [27] reported that the kinetic energy transferred into the material results in plastic deformation. However, this stage is still not well understood as to the definition of the stage, which solely depends on the observer. For this work, the incubation period was defined as the period where mass loss is negligible. At the early stages of the erosion damage (end of incubation period), isolated pits are observed which result in measurable mass loss. The early damage mechanism is discussed in Section 3.4. Table 2 shows the typical incubation period (erosion initiation time) and number of impingements to erosion initiation as well as the maximum erosion rates observed at various speeds.

Table 2
Data from three line characterization of erosion curves for various speeds.

Impact speed (m/s)	Rotational speed (rpm)	Water hammer pressure (MPa)[a]	Erosion initiation time (min)	Number of impingement to initiation × 10^5	$ER_{max} \times 10^{-5}$ (g/min)
150	6000	506	840[b]	302.4[b]	[b]
200	8000	705	340	163.2	1.54
250	10,000	919	45	27.00	12.00
275	11,000	1032	20	13.20	25.00
300	12,000	1148	4	2.88	125.00
325	13,000	1268	2.5	1.95	172.00
350	14,000	1392	1	0.84	333.00

[a] From Eq. (4).
[b] WDE test was stopped due to prolonged testing without any erosion.

From the three line representation analysis, the general trend is that the higher the speed the shorter the incubation period. This was the case for impact speeds from 200 up to 325 m/s. However, it was observed that the incubation periods for speeds of 325 and 350 m/s were close and in the range of seconds. This can be attributed to the severity of the test and the resulting high induced stresses. The observed trends can also be attributed to the increased water hammer pressure and the impact energy with increased impact speed. This observation is in accord with the explanation given by Thiruvengadam and Rudy [25], Ma et al. [17], Mahdipoor et al. [28] and Kamkar [23]. The water hammer pressure is the induced pressure exerted by the "arrested" liquid droplet on the solid surface. This is an important factor that influences the surface damage especially at the incubation stage [17]. According to Heymann [19,29], this pressure can be considerably higher than the yield strength of many alloys especially at high impact speeds. (Eqs. (2)–4) show the different water hammer pressure representations in the literature [19,29].

$$P = \rho CV \tag{2}$$

$$P = \rho CV\left(1 + \frac{KV}{C}\right) \tag{3}$$

$$P = \rho CV\left(2 + \frac{(2K-1)V}{C}\right) \tag{4}$$

where P is the pressure, ρ is the density of the liquid (1000 kg/m^3), C is the acoustic velocity of the liquid (1500 m/s – for water), V is the impact velocity (m/s) and $K = 2$ for water.

These equations are approximations that satisfy wide range of impact speeds on solid surfaces. Eq. (2) represents one-dimensional water hammer pressure developed for liquid-solid impact on a rigid surface. Eq. (3) incorporates the shock wave velocity variable for rigid and elastic surface. Moreover, Eq. (4) provides a reasonably critical impact pressure with the condition that Mach number is greater than 0.2 as reported by Heymann [29]. Therefore, impact speeds equal to or greater than 300 m/s will satisfy the assumption of [29]. Table 2 shows the calculated impact pressure values based on Eq. (4) for different impact speeds. One can see that the impact pressure is proportional to the impact speed and at higher speeds the pressure induces stress that exceeds the yield strength of the material. Sanada's et al. [30] also reported that different pressure distributions are produced at different Mach number (Mi) ranges. They [30] concluded that the difference in pressure at the centre and edge of the droplet is minimized for low Mi (between 0.1 and 0.4). For high Mi (>0.4), the edge pressure is three times that of the centre when jetting starts [31,32]. Therefore, the initiation period will be influenced greatly by the exerted impact pressure as shown in Fig. 7. Fig. 7 also shows that the impact pressure is inversely proportional to the number of impingements to erosion initiation. Zhou et al. [33] showed a linear relationship between water hammer pressure and droplet size. However, in the present work the average droplet size was kept constant.

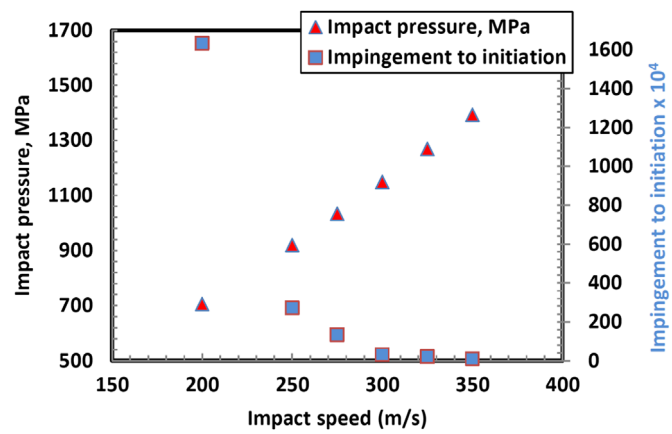

Fig. 7. Relationship between impact speed, impact pressure and erosion initiation.

Fig. 6 shows that reducing the impact speed delayed the erosion initiation time and this was attributed to the reduced impact pressure and impact energy at lower speeds. It is important to note that when lower speeds were used, the erosion time intervals were increased. Therefore, prolonged erosion time corresponding to more water impingements was adapted. For instance, this can be seen for speed test of 200 m/s (Fig. 6a) where the erosion started after 340 min (16.32 million impingements). Even though the reduction of impact speed showed prolonged initiation times, such speeds cannot be used in the mitigation of erosion. These low speeds are not practical in running compressor blades in gas and steam turbines. The present study covered a wide range of impact speeds (150–350 m/s) however, very low speeds (<150 m/s) and very high speeds (>350 m/s) were not tested. The extrapolation of initiation times and maximum erosion rates using the current data might give unsatisfactory results. This is due to the fact that liquid characteristics and target responses vary significantly with impact speeds. Since the erosion rate is not constant with time, prediction of erosion damage would also be difficult. In this case, experimental investigation becomes paramount.

Another point of interest is the threshold speed range (150 m/s $\leq V_{threshold} <$ 200 m/s) that was observed after prolonged time of exposure (up to 840 min for test at 150 m/s). This velocity is the so-called first threshold while the velocity at which mass loss is measurable is the second threshold [24]. However, there is a challenge in understanding this velocity due to the target response, erosion facility, surface quality and the water droplet characteristics such as size, density, impact angle and the frequency of impact. The forgoing point has been mentioned by Rein [34]. Table 3 shows the experimental $V_{threshold}$ values for different materials and applications.

Table 3
Experimental threshold velocities and nth power of velocity by different authors.

S/No.	Material	First threshold speed (m/s)	nth Power of velocity	Ref.
1	S15C-Carbon steel[a]	80	6	[35]
2	STPA22- Alloy steel[a]	90	7	[35]
3	SUS304-Stainless steel[a]	120	7	[35]
4	Al1070, Al5056, C3604, SS400, S20C[a]	–	7[d]	[36]
5	Al-1100[b]	15	5	[25]
6	316SS[b]	45	5	[25]
7	TiAl[c]	200–250	11–13	[18]
8	Ti–6Al–4V[c]	–	9	[23]
9	Ti–6Al–4V[c]	–	7–9	[18]
10	Ti–6Al–4V[c]	$150 \leq V < 200$	> 9	Present study

[a] Liquid impingement erosion for pipe wall thinning.
[b] Liquid jet impact.
[c] Water droplet erosion for compressor blade applications.
[d] Average value for all materials with a scattering from 5–9 depending on material.

One might suggest that for every reported threshold speed, the test conditions should be clearly stated. This is because the first threshold velocity by one researcher might correspond to the second velocity by another researcher. For instance, Thiruvengadam and Rudy [25] defined their threshold velocity as the velocity at which detectable indentations are observed using a 10 × magnifier under suitable lighting. They [25] reported the relationship between the impact (threshold) velocity and the number of impacts after which detectable indentations are observed on Al 1100 and 316SS alloys. After several repeated observations, they [25] showed that the threshold velocities corresponding to 10 million impacts were 15 m/s for Al 1100 and 45 m/s for 316SS (Table 3). In this work, it was found that using average droplet size of 464 μm and flow rate of 0.05 l/min, the threshold velocity was in the range of 150 m/s $\leq V_{threshold} <$ 200 m/s after 840 min of exposure time which corresponds to approximately 30 million impingements. Here, only a shiny erosion line trace was observed under the optical macrograph as shown in the inset of Fig. 6a.

3.2.2. Effect of impact speed on the maximum erosion rate

Immediately after the energy accumulation (acceleration) stage the material loss rate becomes significant up to a maximum. This stage is the zone during which the measured mass loss is at its peak due to fracture and deep craters [25] thus, huge chunks of materials are removed. From Table 2, the influence of impact speed on the maximum erosion rate showed that greater ER_{max} values were recorded at higher speeds. Oka et al. [37] also reported similar trend of maximum damage (erosion) rate at higher impact speeds. For lower speed tests, more exposure time/impingements were required to have an equal mass loss than when using higher speeds. Moreover, it can be suggested here that each impinging droplet causes its own damage during the very high impact speed. Whereas, water accumulation might have decreased the erosion rates in low impact speed test. However, experimental proofs are needed to verify this hypothesis. More so, the energy level is greatly attenuated at lower impact speed than higher impact speed. The ER_{max} and impact speed relationship has been discussed in the literature [25,35]. That is the power law relationship where speed exponents were determined. This relationship between the ER_{max} and impact velocity is derived using Eq. (5).

$$E_R \propto V^n \tag{5}$$

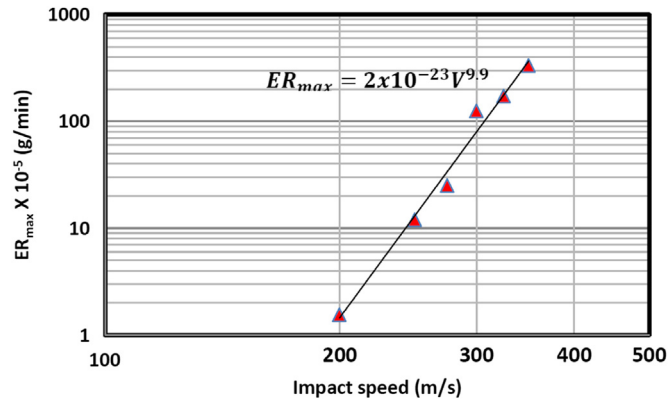

Fig. 8. Log–log graph of ER_{max} *versus* impact speed.

where E_R is the erosion rate, V is the impact speed and n is the speed exponent. Typical speed exponent values for metal are in the range of 5–7 as reported in the literature [25,26,38]. Table 3 shows speed the exponent value for various materials in comparison with the present work. Based on Table 3 and Fig. 8, a different exponent value higher than nine is obtained, which is in accord with Kamkar [23] and Mahdipoor et al. [18]. Thus, this can be attributed to the test conditions, set-up and erosive medium characteristics. Having different material microstructures could reveal different exponent values. The method of ER_{max} determination could also have played a role in this difference [18]. For instance, using the instantaneous erosion rate approach which is the slope between two consecutive points on the WDE curve could give a difference value than that observed when using Fig. 4. Even though erosion rate is sensitive and proportional to the impact speed (generally erosion conditions) [18], no satisfactory explanation for the relationship between the erosion rate and impact velocity has been provided in the literature yet. This could be due to the fact that other parameters such as the droplet size, droplet velocity and the target materials properties also play significant roles in the erosion process. For instance, Mahdipoor et al. [18] reported different speed exponent values for Ti–6Al–4V tested with different droplet sizes. Values of 8.9 and 7.7 were observed for droplet size of 463 and 603 μm, respectively. Also, Ikohagi [39] mentioned the influence of liquid film on the erosion rate. He [39] studied the numerical simulation of single droplet (100 μm size) impingement on a solid surface. He [39] found that the exponent value (n) increased from 5.3 to 7.7 for the solid surface with a liquid film of 2.5 μm thickness. Fujisawa et al. [40] further showed in their experimental work combined with theoretical consideration that increase in the liquid film thickness increases the damping effect of the impact pressure. Hence, thicker liquid film shows reduced erosion rates and this is in accord with the suggestion by Ikohagi [39]. The works in [18,39,40] clearly indicate that speed exponent is function of droplet size and the entire testing conditions. Therefore, accounting for the effect of all these parameters might be tedious. Thus, different exponent values might be observed.

3.3. Optical macrographs of eroded coupons

To demonstrate and understand how the erosion process evolved and progressed, optical macrographs were taken after each interval during testing. This is also the interval during which the coupon is weighed and the mass loss is recorded. Fig. 9a–c shows the erosion evolution and procession for the tested Ti–6Al–4V coupons at impact speeds of 250, 300 and 350 m/s, respectively. Normally, the erosion process initiates with an erosion trace line due to impingement of droplets [16,17]. Fig. 9a shows this initiation process after 20 minutes of exposure time at 250 m/s where the

mass loss is negligible. This stage is reported as the region of local plastic deformation that causes grain displacement leading to formation of microcracks [27] and depressions [41]. After a few additional impacts, small pits are formed along the erosion trace line and with further impacts, large isolated pits are formed and gradual pit growth is observed. This is the situation seen in Fig. 9a after 50 min of exposure time where mass loss of 0.0007 g was recorded. After 65 min, the acceleration stage was reached where significant mass loss of 0.0026 g was observed due to the pit coalescence and secondary cracks intersecting thereby, detaching larger pieces of material [11,23]. The maximum erosion rate (0.000213 g/min) was reached after 80 min where material damage was at its peak and complete crater has been formed. The material damage was due to high pressure exerted and the liquid lateral jetting. The jetting is the radial outflow of the liquid droplets after impact which is identified as a major cause of the erosion damage [42]. This jetting also interacts with surface discontinuities [31] thereby, forming surface cracks and surface asperities. This leads to significant removal of material during the advanced erosion stages. It is important to note that with increased exposure time and a severe erosion test (for instance, increase in impact speed), both depth and width of the craters are increased [17]. For instance, crater width of less than 1mm and more than 1mm were observed after 65 and 310 min, respectively (Fig. 9a). This observation is also true when comparing the crater width/depth for different speeds at the same exposure time and this is in accord with the findings of [23]. Similarly, Fig. 9b and c show that increasing the impact speed accelerated the erosion evolution and progression as compared to Fig. 9a. For instance, measureable mass losses were observed after 8 and 2 minutes of exposure only at 300 m/s (Fig. 9b) and 350 m/s (Fig. 9b), respectively. Maximum erosion rates were 0.001125 g/min and 0.00245 g/min after 12 and 5 min of exposure at 300 m/s and 350 m/s,

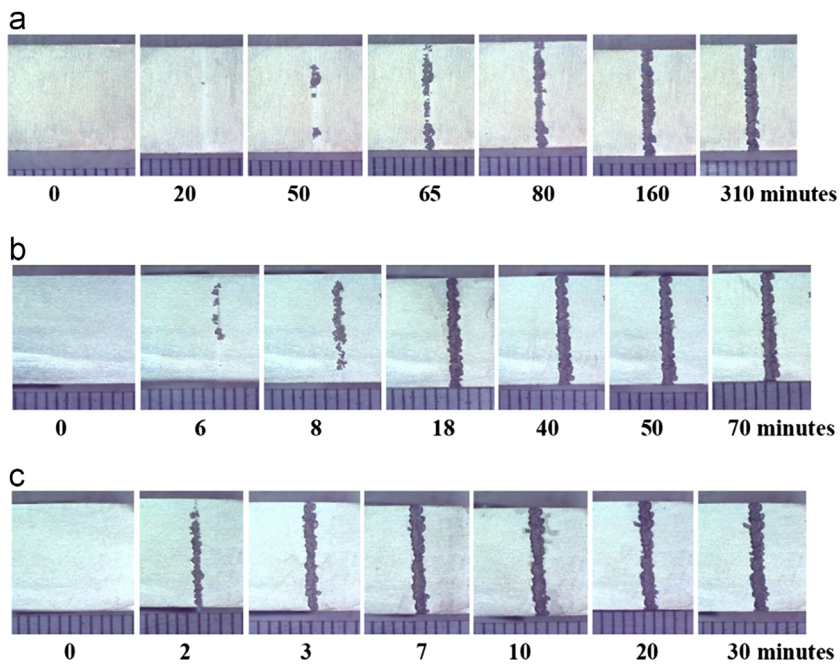

Fig. 9. Optical macrographs showing the erosion evolution and progression on Ti–6Al–4V coupon tested at (a) 250 m/s (b) 300 m/s and (c) 350 m/s.

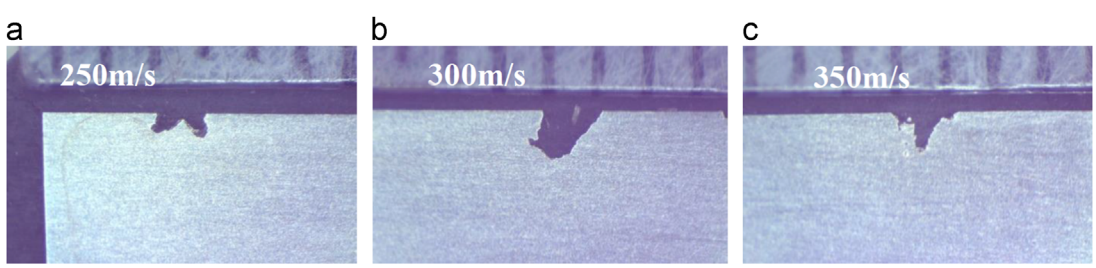

Fig. 10. Macrographs showing the influence of impact speeds on the observed crater width and depth.

Table 4
Summary of the observed accumulated material loss, crater width and depth at different speeds.

Impact Speed (m/s)	Experiment stopped after		Accumulated material loss (g)	Crater width (mm)	Crater depth (mm)
	Exposure time (min)	No. of impingements × 10^5			
250	415	249	0.0237	1.09	0.50
300	70	50	0.0269	1.28	1.08
350	30	25	0.0353	1.44	1.00

respectively. Full crater was formed after 3 min at 350 m/s compared to the full crater formation after 80 min at 250 m/s. Therefore, Fig. 9a–c show the influence of changing the impact speed on the erosion behaviour. The early erosion initiation and progression at high impact speed is attributed to the increased impact pressure which induced significant stresses.

To further understand the influence of impact speed on the erosion crater behaviour; the accumulated material loss, crater width and depth were observed after certain exposure times/number of impingements at different impact speeds. Fig. 10 shows the polished cross-sectional views of the erosion craters at impact speeds of 250, 300 and 350 m/s halted after 415, 70 and 30 min, respectively. Prolonged exposure time was chosen for low impact speed (250 m/s) in order to have significant mass loss for better comparison. The crater widths and depths were measured with the aid of a microscope. The accumulated material losses, crater widths and depths are presented in Table 4. It can be seen from Table 4 that increasing only the impact speed showed significant mass loss and increase in crater dimensions even with fewer number of impingements/exposure time. For instance, the test at 350 m/s which was halted after 30 min (after 25×10^5 impingements) showed 48.9% and 31.2% increase in mass loss as compared to test at 250 m/s (after 249×10^5 impingements) and 300 m/s (after 50×10^5 impingements), respectively. Similarly, increasing the impact speed from 250 m/s to 350 m/s showed a 32% and 100% increase in crater width and depth, respectively. It is worth noting that the number of impingements for test at 250 m/s is 10 times more than test at 350 m/s. It should also be noted that the crater depth might vary depending on the location of the cross-section. This is the case shown in Fig. 10b and c where 350 m/s test showed less depth compared to 300 m/s test. Based on several cross-sectional views taken, similar trends were observed especially for the accumulated mass loss and crater depth. For instance, another set of craters were sectioned after 18.6×10^5, 50×10^5 and 30×10^5 impingements at 250, 300 and 350 m/s, respectively. Accumulated mass losses were 0.017, 0.0264 and 0.0391 g, respectively. Crater depths of 0.392, 0.769 and 0.841 mm were observed, respectively. This observation is in general agreement with the data in Table 4 which indicates a linear relationship between the impact speed and observed crater depth. Moreover, the significant mass losses observed at high impact speed (350 m/s) could suggest that the crater dimensions are highly representative. As mentioned previously, this is attributed to the increased test severity, which induces high stresses. This can also be attributed to the change in droplet properties with increase in test severity [16].

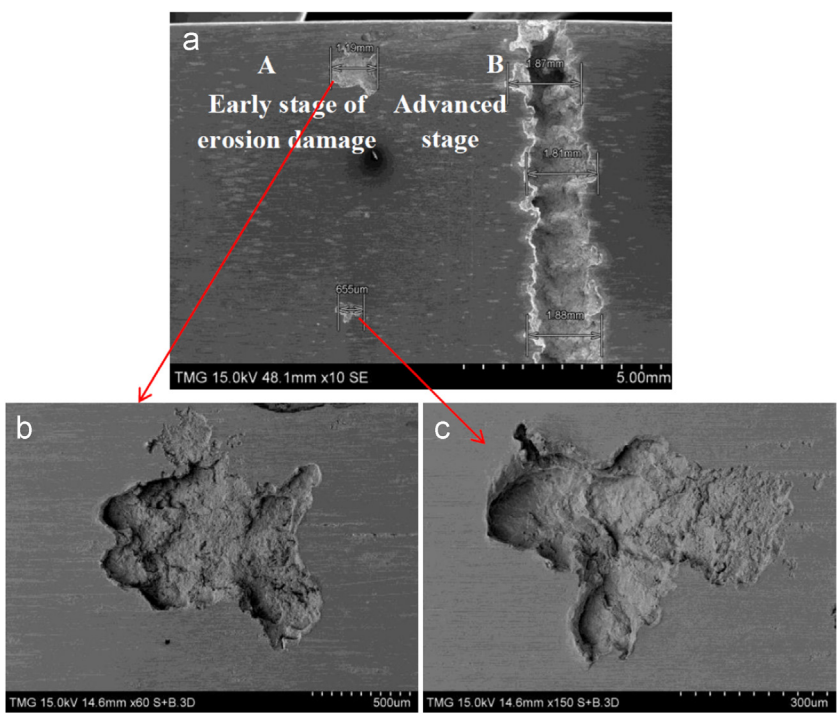

Fig. 11. SEM showing (a) typical erosion initiation and advanced erosion stages and (b, c) isolated pits during early stages of erosion damage.

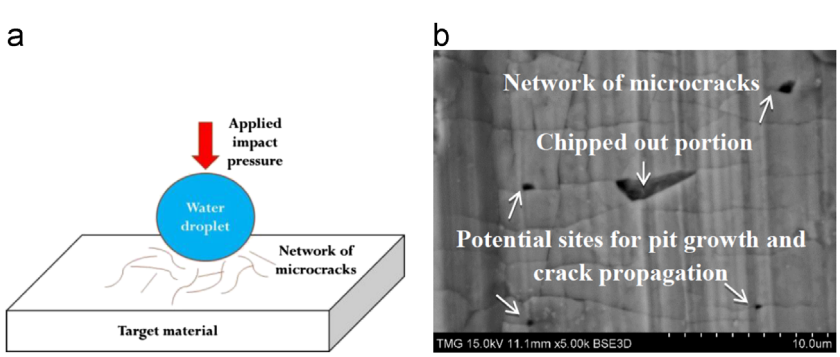

Fig. 12. Shows the formation of cracks due to droplet impacts (a) and typical network of microcracks (b).

3.4. Erosion mechanism

The WDE phenomenon sets-up different material removal mechanisms at various stages of the erosion process. This damage will also depend on the material nature – whether it is brittle or ductile, for *example*. However, the material removal is not well understood due to the difficulty in accurately predicting the hydrodynamic condition that causes particular erosion damage [11]. The individual stages during the erosion process merge into one another without any noticeable transition. For this reason, the present investigation carefully explored the important stages of the erosion such as the early stage of erosion damage (damage initiation stages) and advanced stages as shown in Fig. 11. Regions A and B in Fig. 11a represents the early stages of the damage and advanced stages, respectively. Fig. 11b and c shows the isolated pits during the early stages. It is important to note that at a moderate impact speed test (200–300 m/s) more apparent features can be observed as compared to a severe test. Based on the forgoing point, SEM images revealed several features obtained from different WDE tested conditions. This is to fully understand the mechanism of material removal during the erosion process.

3.4.1. Early stages of erosion damage

Based on the SEM observations, it was found that the formation of a shiny erosion line, isolated erosion pits of different dimensions, asperity formation and network of microcracks were the predominant features during the damage initiation period. Other features such as grain tilting resulting in grain boundary damage were also reported by Kamkar [23]. Nevertheless, as pointed out earlier, the definition of incubation stage (start and end) depends on the observer and this might vary significantly. For instance, it was believed that when the plastic deformation limit is reached and with more energy (kinetic energy) supplied to the target, erosion initiation starts [42,43]. It is worth noting that for plastic deformation to occur, the dynamic yield strength of the target material must be exceeded [44]. The plastic deformation induces high local concentration of crystalline defects, which induce high internal stresses [43]. With more droplet impacts surface damages such as the microcracks are observed. The initiation of microcracks is an important feature observed at the on-set of the erosion process. Rieger [43] reported that the crack formation occurs when the fracture strength is exceeded. Kamkar [23] reported that the cracks formed due to the high local deformation with conditions related to low cycle fatigue (LCF). Ma et al. [17] attributed the

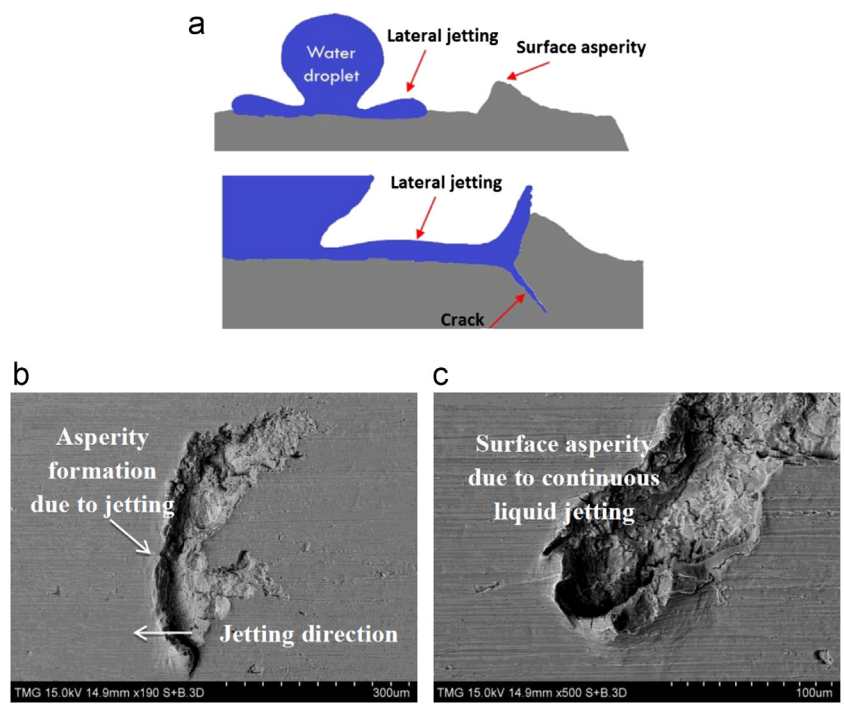

Fig. 13. Formation of surface asperity [42] (a) typical surface asperities after few impacts (b) and accumulated impacts and continuous lateral jetting (c).

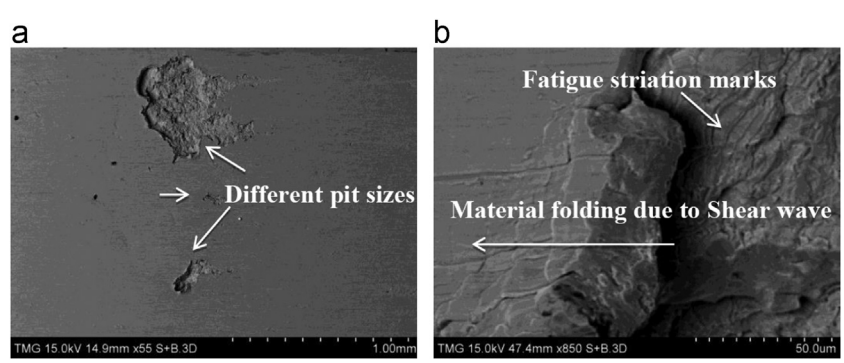

Fig. 14. SEM micrographs showing (a) different pit sizes and (b) material folding and fatigue striation marks.

formation of surface microcracks to synergetic effect of water hammer pressure and stress waves. Fig. 12a shows how the crack lines are formed due to the repeated droplet impacts. Fig. 12b shows a typical network of microcracks that was observed and this can be attributed to the aforementioned reasons given by [17,23,43]. These microcracks chip out small amount of material leading to a stress raiser that initiates more rapid failure due to repetitive impacts with sufficient magnitude [24,45]. It is evident from Fig. 12b that microcracks during the early stages of damage serve as potential sites for favourable pit coalescence and growth and crack propagation [12]. Thus, detachment of larger fragments occurs at later stages in the erosion process due to following impacts and liquid lateral jetting.

Also, water impingement results in surface depressions, which are typical trademarks associated with the incubation period [41,46–49]. These depressions are most likely to be observed at low impact velocities whose impact pressures induce stresses greater than the yield strength of the material [50]. At high velocities, the formed depressions might not be seen due to the severity of the test. Field et al. [51] pointed out that these depressions are enlarged with further impacts and in turn produce surface asperities due to repeated liquid lateral jetting. Heymann [42] stated that the high-speed lateral jetting interacts with surface irregularities or asperities thereby, causing further crack initiation and damage. Also, Hattori et al. [35] mentioned that these asperities are the reasons for the fatigue crack initiation and material removal. Fig. 13a shows the formation of surface asperities as explained by [42]. Fig. 13b and c shows surface asperities observed during the early stages of the erosion damage after few droplet impacts and accumulated impacts. Fig. 13c indicates that the asperities further open-up with increased impacts thus, leaving a large cavity on the surface that deepens with time [42]. Here, removal of material by the shearing or tearing mode was observed.

During the erosion initiation stage, isolated pits of irregular shapes and dimensions were found as shown in Figs. 11b and c and 14a. This could possibly suggest the irregularity of the erosion process and the initial surface quality such as different surface imperfections. With repeated impacts on the pits, deeper and wider craters are formed thereby, leading to the advanced erosion stage where significant material is lost. The phenomenon of compression and shear waves is also paramount in understanding the erosion damage. According to the elastic wave theory of solids [52], "when an impulse loading acts on a solid surface, a compression and a shear wave are generated in the bulk solid and on the surface, a Rayleigh surface wave is generated" [31]. As the compression wave travels along a free surface, shear (head) wave is formed. The shear wave offsets the stresses caused by the compression wave. Shi and Dear [53] stated that the liquid lateral jetting causes energetic shear waves in the solid thereby, forming shear bands in sub-layer of materials. Field et al. [54] reported that the Rayleigh wave forms circumferential cracks as the liquid jets away. In this WDE study, the droplet impact causes the compression wave while the lateral jetting causes the shear wave. The material folding/upheaving shown in Fig. 14b could be due to the shear waves. Also, fatigue striation marks are also shown which indicates the fatigue-like damage.

These fatigue striation marks are due to the fatigue-based damage caused by cyclic nature of the liquid droplets [17,23,35]. Similar features (material folding and striation marks) were also observed at the advanced stages of the erosion process [17]. In general, the erosion initiation stage strongly depends on magnitude, duration and frequency of the localized loadings as well as the material's response [45], microstructure [42] and surface quality (roughness) [16,24].

3.4.2. Advanced erosion stage

The advanced stage in this study is shown as region "B" in Fig. 11a. Fig. 15 shows several damage features observed during the advanced erosion stage. A significant amount of material was lost due to water droplets impingements. This loss of large chunks of material was due to the hydraulic penetration as indicated by the arrow in Fig. 15b. This is the penetration of liquid over pre-existing cracks or pits thus, forcing large chunks of material to be removed. Moreover, the hydraulic penetration phenomenon has been observed and reported as the most profound material removal mode in Ti–6Al–4V [14,17,28,55,56]. Fig. 15b also revealed how a sub-surface crack

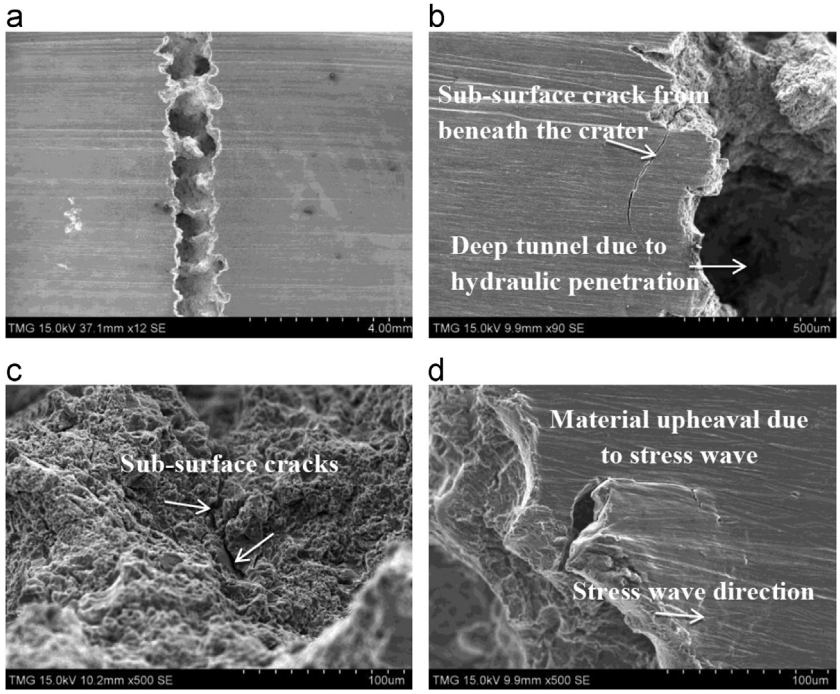

Fig. 15. SEM showing eroded Ti–6Al–4V coupon during the advanced erosion stage.

emanated and propagated from beneath the erosion crater to the top surface. This could be due to the interaction of the impacting droplets with sub-surface defects such as cracks. Typical cracks were observed as indicated by the arrows in Fig. 15c. These cracks could have originated from highly stressed points or damaged grain boundaries. It has been reported that materials are more susceptible to erosion damage if imperfections are present at the grain boundaries [57]. This causes large detachment of grains which leaves a deep void. Material upheaving at the edge of the crater was observed as shown in Fig. 15d. Adler and Vyhnal [56] observed this material upheaving in their rain erosion experiment and attributed it to the merging of cracks which originated from the erosion pits. However, this can also be attributed to the shear wave propagation due to the lateral (radial) jetting of the liquid.

It is imperative to show the crater depths and possible interaction between the formed craters at longer erosion times. This approach of observing multiple craters presented in this study might give better understanding with regard to material removal mechanisms as WDE progresses. Hence, crater geometry, interactions and mean depth of craters can be observed fully. Fig. 16a–c shows the crater cross-section A–A and the in-depth microstructural features, respectively. One can see different crater depths and geometries (spherical and V-shaped crater at points 1, 2 and 3). These can be attributed to the hydraulic penetration and

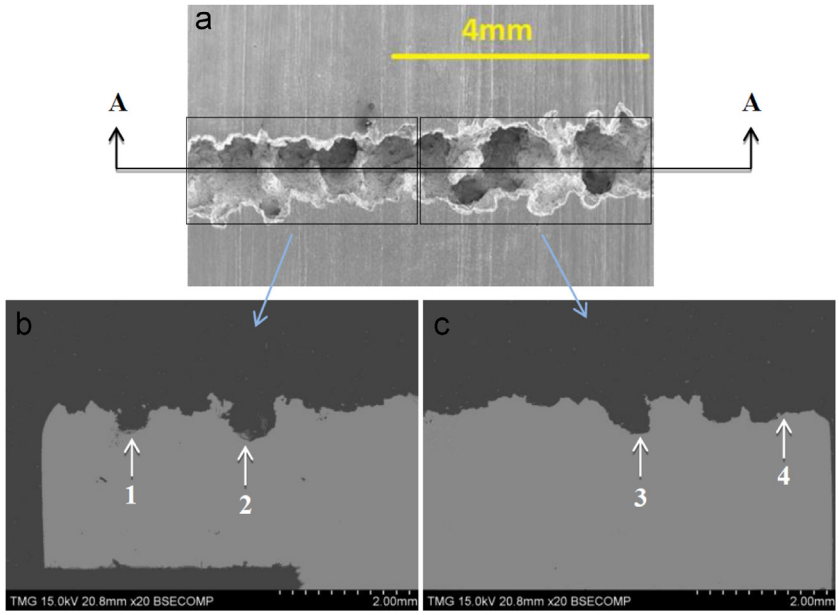

Fig. 16. (a) The crater section A–A and (b) the in-depth microstructural view during the advanced erosion stage.

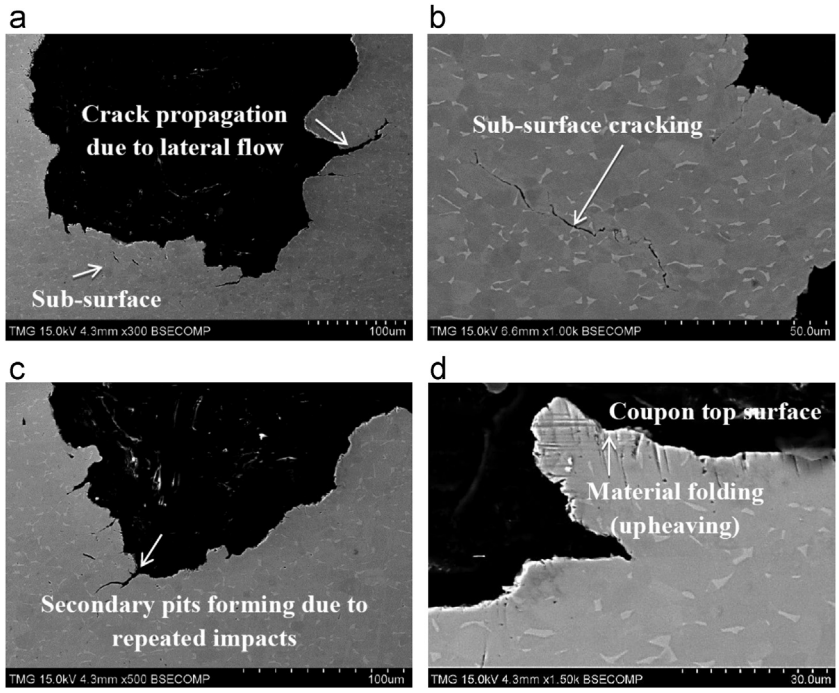

Fig. 17. Erosion crater showing (a) sub-surface cracks and propagation on the sidewall and base, (b) sub-surface cracking (c) secondary pits formation due to high cumulative impacts, and (d) material upheaving/folding.

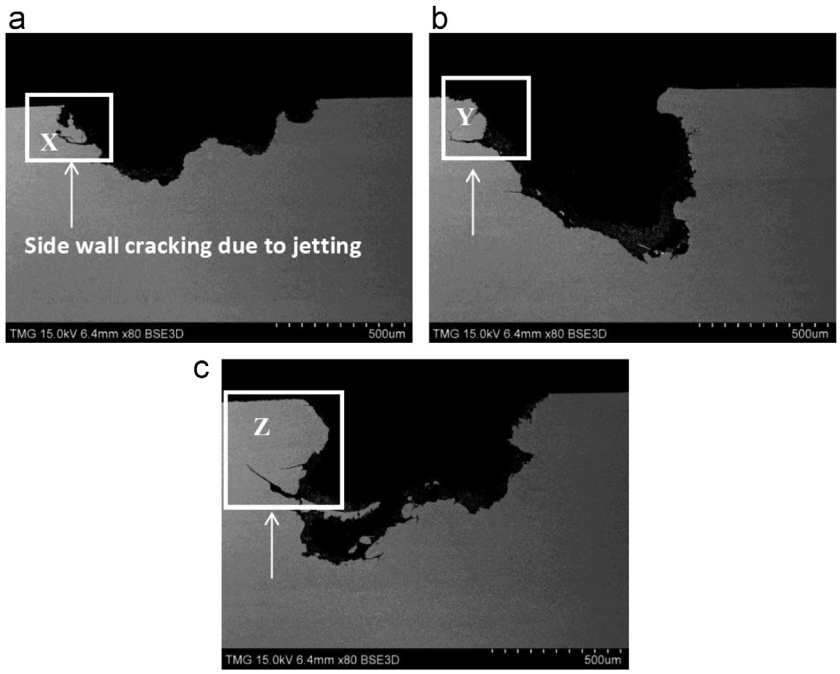

Fig. 18. SEM micrographs showing craters at (a) 250 m/s (b) 300 m/s and (c) 350 m/s.

the irregularity of the erosion process. The deeper craters might have been the initially damaged locations thereby, forming deeper pits and sub-tunnels due to accumulated impacts and lateral jetting, respectively. Other locations (point 4 for instance) showed relatively levelled surface as compared to points 1, 2 and 3. This also confirms the explanation given in Section 3.3 that the crater depth might vary significantly. The variation in the crater geometries and depths could be additional contributions to the difficulty in fully understanding the process of material damage by erosion.

Looking closer at the craters shown in Fig. 16b and c, several other features could be observed. For instance, sub-surface cracks and side wall cracks were observed as shown in Fig. 17a and b. The sub-surface cracking is a direct consequence of the continuous droplet impact. The continuous impact allows for the interaction between the transmitted (compression) and reflected (tension) stress waves which occurs repeatedly [17]. This leads to the initiation of sub-surface cracks and the propagation of existing cracks. This cracking could be intergranular or transgranular or the combination of both in Ti alloys [18,57–59]. Also, due to repeated droplet impacts on existing cavities, secondary pits shown in Fig. 17c are formed and these are termed as sub-tunnels within the craters [42]. This sub-tunnelling phenomenon has been described and observed by Hammitt and Heymann [11], Mahdipoor et al. [59] and Kamkar et al. [23]. Furthermore, Fig. 17d shows the material upheaving/folding due to the stress wave and this is in accord with the top surface feature shown in Figs. 14c and 15d.

Fig. 18a–c shows micrographs taken after 54×10^5, 17×10^5 and 8.4×10^5 impingements at 250, 300 and 350 m/s, respectively. Fig. 18a–c shows side wall cracks which are caused by the liquid lateral jetting. With increased droplet impacts, these side wall cracks propagate removing large chunk of material. This could further highlight the reason why the crater dimensions (width and depth) were increased with increased exposure and severity. For instance, locations X, Y and Z in Fig. 18 indicate vulnerable portions of the material to be removed with increased impacts. Location Z is the largest portion to be removed compared to X and Y. This could account for the significant mass losses observed when using high impact speeds. Depending on the severity of the test, the liquid jetting effect might show different crater geometries. Hence, observing the influence of the impact speed on this jetting will be paramount. It can be seen from Fig. 18a–c that the lateral jetting is more apparent with increasing the impact speed even with relatively low number of impingements/less exposure time. For instance, Fig. 18a shows that the liquid jetting effect seems to be evenly distributed in the crater for mild erosion conditions ($\leq$250 m/s, for instance). However, Fig. 18b and c shows more jetting effect on one side for more severe test conditions ($\geq$300 m/s). This phenomenon has been observed in several micrographs taken at different erosion conditions. This observation is in accord with the claims made by Lesser and Field [60] that the response of liquid droplet changes corresponding to changes in impact speed. They [60] stated that "if the impact speed is sufficiently low for a given liquid, distinct shocks and high-speed jetting would not be expected" and vice versa.

Comparatively, the material damage, crater dimensions and surface features during the early stages of erosion damage and advanced stages are different. For instance, during the advanced stage, the crater deepens further while the width has a slow increase with further impacts. This was not the case during the erosion initiation and subsequent stages where both the crater width and depth increased with more impacts.

4. Conclusion

The WDE behaviour of Ti–6Al–4V and the mechanism of material removal during the early and advanced stages of erosion damage were studied. The following conclusions could be drawn from this study:

(1) Increasing the impact speed decreases the erosion initiation time and increases the maximum erosion rates (ER_{max}). It was also observed that ER_{max} increases with the 9 to 10th power of impact speed. A threshold velocity range between 150 and 200 m/s was observed after 840 min of exposure time corresponding to 30 million impingements.

(2) Erosion crater dimensions were found to increase with increasing impact speed even at significantly lower number of impingements/exposure time compared to low speed.
(3) Early stage of the erosion damage was mainly limited to the generation of microcracks, isolated pits and formation of asperities.
(4) During the advanced stage, the most profound mode of material removal was the hydraulic penetration. Fatigue striation, side wall cracks, sub-surface cracks, material folding and upheaving were also observed at the advanced stage. Impact speed significantly influences the liquid lateral jetting at the advanced water droplet erosion stage.

Acknowledgement

The authors appreciate the efforts made by Jie Yi for measuring the droplet sizes in TMG Lab at Concordia University. The efforts of Hany Kirols, Mohammad Mahdipoor and Ahmad Mostafa are highly appreciated. The authors gratefully acknowledge the financial support provided by Concordia University, Canada (Frederick Lowy Scholars Fellowship Award, Graduate Student Support Programme (GSSP) - Grant Number VE0103 and Research Assistanship (RA) - Grant Number L00264 Funds).

References

[1] C. B. Meher-Homji, T. R. Mee, Gas turbine power augmentation by fogging of inlet air. in: Proceedings of 28th Turbomachinery Symposium, ASME International, Houston, Texas, USA, 4th September 1999, pp. 93–114.
[2] Energy Information Agency: 2005 Database of U.S Department of Energy, Available online: ⟨http://energy.gov/data/open-energy-data⟩, 28 October, 2013.
[3] D. Punwani, Turbine inlet cooling: an energy solution that's better for the environment, ratepayers and plant owners, Presented at POWER-GEN International, Orlando, Florida, USA, 2nd December, 2008, pp. 1–9.
[4] S. Duncan, Thermal energy storage and its effect on CO_2 at the Source. Presentation at 2007 ASHRAE technical committee summer meeting, Long Beach, California, USA, 23–27th June 2007.
[5] T. Giampaolo, The Gas Turbine Handbook: Principles and Practice, 3rd ed., Fairmont Press, New York, USA, 2006.
[6] J.R. Khan, Fog Cooling, Wet Compression and Droplet Dynamics in Gas Turbine Compressors (Ph.D. dissertation), University of New Orleans, USA, 2009.
[7] K.G. Budinski, M.K. Budinski, Engineering Materials-Properties and Selection, 9th Ed., Prentice Hall, New York, USA, 2010.
[8] N. Fujisawa, R. Morita, A. Nakamura, Critical consideration on wall thinning rate by liquid droplet impingement erosion, E-J. Adv. Maint. 4 (2) (2012) 79–87.
[9] S. Yerramareddy, Effect of operational variables, microstructure and mechanical properties on the erosion of Ti–6Al–4V, Wear 142 (1) (1991) 253–263.
[10] ASTM G73-10, Standard test method for liquid impingement erosion using rotating apparatus, ASTM International, West Conshohocken, PA, 2010, Available online: ⟨www.astm.org⟩.
[11] F.G. Hammitt, F.J. Heymann, Liquid-erosion failures, failure analysis and prevention, ASM handbook, ASM International, vol. 11, 1986, pp. 163–171.
[12] B. Luiset, F. Sanchette, A. Billard, D. Schuster, Mechanisms of stainless steels erosion by water droplets, Wear 303 (1–2) (2013) 459–464.
[13] C. Gerdes, A. Karimi, H. Bieler, Water droplet erosion and microstructure of laser nitrided Ti–6A1–4V, Wear 186–187 (1995) 368–374, Part 2.
[14] B.S. Mann, Water droplet and cavitation erosion behavior of laser treated stainless steel and titanium alloy: their similarities, J. Mater. Eng. Perform. 22 (12) (2013) 3647–3656.
[15] F.J. Heymann, Toward quantitative prediction of liquid impact erosion, Characterization and determination of erosion resistance, ASTM STP 474, American Society for Testing Materials, 1970, pp. 212–248.
[16] H.S. Kirols, D. Kevorkov, A. Uihlein, M. Medraj, The effect of initial surface roughness on water droplet erosion behaviour, Wear 342–343 (2015) 198–209.
[17] D. Ma, A. Mostafa, D. Kevorkov, P. Jedrzejowski, M. Pugh, M. Medraj, Water impingement erosion of deep-rolled Ti64, Metals 5 (3) (2015) 1462–1486.
[18] M.S. Mahdipoor, H.S. Kirols, D. Kevorkov, P. Jedrzejowski, M. Medraj, Influence of impact speed on water droplet erosion of TiAl compared with Ti–6Al–4V, Scientific Reports, vol. 5, 2015, Article no. 14182 (17 pages).
[19] F. Heymann, Liquid impingement erosion, ASM handbook, Materials Park, OH, ASM International, vol. 18, 1992, pp. 221–232.
[20] V.A. Ryzhenkov, A.I. Lebedeva, A.F. Mednikov, Erosion wear of the blades of wet–steam turbine stages: present state of the problem and methods for solving it, Therm. Eng. 58 (9) (2011) 713–718.
[21] M. Ahmad, M. Casey, N. Sürken, Experimental assessment of droplet impact erosion resistance of steam turbine blade materials, Wear 267 (9–10) (2009) 1605–1618.
[22] B.S. Mann, V. Arya, An experimental study to corelate water jet impingement erosion resistance and properties of metallic materials and coatings, Wear 253 (5–6) (2002) 650–661.
[23] N. Kamkar, Water Droplet Erosion Mechanisms of Ti–6Al–4V (Ph.D. dissertation), École de Technologie Supérieure (ÉTS), Montreal, QC, Canada, 2014.
[24] F. Heymann, On the time dependence of the rate of erosion due to impingement or cavitation, ASTM STP 408, American Society for Testing and Materials, 1967, pp. 70–110.
[25] A. Thiruvengadam, S.L. Rudy, Experimental and analytical investigations on multiple liquid impact erosion, Natl. Aeronaut. Space Adm. (NASA) (1969) 1–93.
[26] G. Hoff, G. Landbein, H. Rieger, Material destruction due to liquid impact in erosion by cavitation or impingement, in: Proceedings of the symposium presented at the 6–9th Annual Meeting, American Society for Testing and Materials, Atlanta City, New Jersey, 26th June–1st July 1966, pp. 42–69.
[27] T. Keil, P.F. Pelz, J. Kadavelil, J. Necker, W. Moser, D. Christ, Droplet impact versus cavitation erosion Warwick innovative manufacturing research center (WIMRC), in: Proceedings of the 3rd International Cavitation Forum, University of Warwick, UK, 2011, pp. 1–8.
[28] M.S. Mahdipoor, F. Tarasi, C. Moreau, A. Dolatabadi, M. Medraj, HVOF sprayed coatings of nano-agglomerated tungsten-carbide/cobalt powders for water droplet erosion application, Wear 330–331 (2015) 338–347.
[29] F. Heymann, High speed liquid impact between a liquid drop and a solid surface, J. Appl. Phys. Vol. 40 (No. 13) (1969) 5113–5122.
[30] T. Sanada, K. Ando, T. Colonius, A computational study of high-speed droplet impact, Fluid Dyn. Mater. Process. 7 (4) (2011) 329–340.
[31] S. Honghui, J.E. Field, Stress waves propagation in solids under high-speed liquid impact, Sci. China Ser. G Phys. Mech. Astron. 47 (6) (2004) 752–766.
[32] J.E. Field, The physics of liquid impact, shock wave interactions with cavities and the implications to shock wave lithotripsy, Phys. Med. Biol. 36 (11) (1991) 1475–1484.
[33] Q. Zhou, N. Li, X. Chen, T. Xu, S. Hui, D. Zhang, Analysis of water drop erosion on turbine blades based on a nonlinear liquid–solid impact model, Int. J. Impact Eng. 36 (9) (2009) 1156–1171.
[34] M. Rein, Phenomena of liquid drop impact on solid and liquid surfaces, Fluid Dyn. Res. 12 (2) (1993) 61–93.
[35] S. Hattori, M. Takinami, Comparison of cavitation erosion rate with liquid impingement erosion rate, Wear 269 (3–4) (2010) 310–316.
[36] N. Fujisawa, T. Yamagata, S. Takano, K. Saito, R. Morita, K. Fujiwara, F. Inada, The influence of material hardness on liquid droplet impingement erosion, Nucl. Eng. Des. 288 (2015) 27–34.
[37] Y.I. Oka, S. Mihara, H. Miyata, Effective parameters for erosion caused by water droplet impingement and applications to surface treatment technology, Wear 263 (1–6) (2007) 386–394.
[38] N. Fujisawa, T. Yamagata, K. Hayashi, T. Takano, Experiments on liquid droplet impingement erosion by high-speed spray, Nucl. Eng. Des. 250 (2012) 101–107.
[39] T. Ikohagi, On evaluation of LDI erosion rate based on fluid/solid coupled simulation, in: Proceeding of 8th International Conference Flow Dynamics, 2011, pp. 402–403.
[40] N. Fujisawaa, T. Yamagata, K. Saito, K. Hayashi, The effect of liquid film on liquid droplet impingement erosion, Nucl. Eng. Des. 265 (2013) 909–917.
[41] L. Huang, J. Folkes, P. Kinnell, P.H. Shipway, Mechanisms of damage initiation in a titanium alloy subjected to water droplet impact during ultra-high pressure plain waterjet erosion, J. Mater. Process. Technol. 212 (9) (2012) 1906–1915.
[42] F.J. Heymann, Erosion by liquids, Mach. Des. (1970) 118–124.
[43] H. Rieger, The damage to metals on high speed impact with water drops, in: A. A. Fyall, R.B. King (Ed.), Proceedings of the Rain Erosion Conference held at Meersburg, Royal Aircraft Establishment, Farnborough, England, 1965, pp. 107–113.
[44] A.K. Gujba, M. Medraj, Laser peening process and its impact on materials properties in comparison with shot peening and ultrasonic impact peening, Materials 7 (12) (2014) 7925–7974.
[45] W.F. Adler, Analysis of particulate erosion, Wear 37 (2) (1976) 345–352.
[46] G.F. Schmitt, Liquid and Solid Particle Impact Erosion: Technical Report, Air Force Materials Laboratory, Wright Patterson, Air Force Base, Ohio, USA, 1979, AFML-TR-79-4122.
[47] A. Arbor, S. Hattori, M. Takinami, T. Otani, Comparison of cavitation erosion rate with liquid impingement erosion rate, in: Proceedings of the 7th International Symposium on Cavitation, Ann Arbor, Michigan, USA, 17–22nd August 2009, Paper no. 32, pp. 1–6.
[48] J.E. Field, J.J. Camus, M. Tinguely, D. Obreschkow, M. Farhat, Cavitation in impacted drops and jets and the effect on erosion damage thresholds, Wear 290–291 (2012) 154–160.
[49] J. Foldyna, J. Klich, P. Hlaváček, M. Zeleňák, J. Ščučka, Erosion of metals by pulsating, Water Jet. Teh. Vjesn. 2 (2012) 381–386.
[50] G.P. Thomas, The initial stages of deformation in metals subjected to repeated liquid impact, Philos. Trans. A Royal Soc. Lond. 260 (1996) 140–143.
[51] J. E. Field, M. B. Lesser, J. P. Dear, Studies of two-dimensional liquid-wedge impact and their relevance to liquid-drop impact problems, in: Proceedings of

the Royal Society of London, Series A, Mathematical and Physical Sciences, London, UK, 8th October 1985, vol. 401(1821), pp. 225–249.
[52] K.F. Graff, Wave Motion in Elastic Solids, Dover Publications, Inc., New York, 2012.
[53] H.H. Shi, J.P. Dear, Oblique high-speed liquid–solid impact, Jpn. Soc. Mech. Eng. 35 (3) (1992) 285–295.
[54] J. E. Field, D. A. Gorham, J. T. hagan, M. J. Mattewson, M. V. Swain, S. Van der Zwaag, Liquid jet impact and damage assessment for brittle solids, in: Proceedings of the 5th International Conference on Erosion by Solid and Liquid Impact, Cambrigde, UK, 3–6th September 1979, pp. 1–11.
[55] J.I. Robinson, R.C. Reed, Water droplet erosion of laser surface treated Ti–6Al–4V, Wear 187 (1995) 360–367.
[56] W. F. Adler, R. F. Vyhnal, Rain erosion of Ti–6Al–4V. in: Proceedings of the 4th International Conference on Rain Erosion and Associated Phenomena, Meersburg, Germany, 8–10th May 1974, pp. 536–569.
[57] M.C. Kong, D. Axinte, W. Voice, Aspects of material removal mechanism in plain waterjet milling on gamma titanium aluminide, J. Mater. Process. Technol. 210 (3) (2010) 573–584.
[58] V.A. Joshi, Titanium Alloys: An Atlas of Structures and Fracture Features, CRC Press, Taylor & Francis Group, USA, 2006.
[59] M.S. Mahdipoor, D. Kevorkov, P. Jedrzejowski, M. Medraj, Water droplet erosion mechanism of nearly fully-lamellar gamma TiAl alloy, Mater. Des. 89 (2) (2015) 81–87.
[60] M.B. Lesser, J.E. Field, The impact of compressible liquids, Ann. Rev. Fluid Mech. 15 (1983) 97–122.